Applied Surface Science 515 (2020) 146084

Contents lists available at ScienceDirect

Applied Surface Science

journal homepage: www.elsevier.com/locate/apsusc

Full Length Article

Boron addition in a non-equiatomic $Fe_{50}Mn_{30}Co_{10}Cr_{10}$ alloy manufactured by laser cladding: Microstructure and wear abrasive resistance

Jose Y. Aguilar-Hurtado[a,b,c,*], Alejandro Vargas-Uscategui[a,d,*], Katherine Paredes-Gil[e], Rodrigo Palma-Hillerns[a], Maria J. Tobar[f], Jose M. Amado[f]

[a] Mechanical Engineering Department, Faculty of Mathematical and Physical Sciences, University of Chile, Beauchef 851, Santiago, Chile
[b] Chemical Engineering, Biotechnology and Materials, Faculty of Mathematical and Physical Sciences, University of Chile, Beauchef 851, Santiago, Chile
[c] CSIRO – Chile International Center of Excellence, Tupper Av. 2007, Santiago, Chile
[d] CSIRO Manufacturing, Gate 5, Normanby Road, Clayton, VIC 3168, Australia
[e] Programa Institucional de Fomento a la Investigación, Desarrollo e Innovación, Universidad Tecnológica Metropolitana, Ignacio Valdivieso 2409, P.O. Box 8940577, San Joaquín, Santiago, Chile
[f] University of A Coruña, Industrial Engineering Department II, Laser Applications Laboratory, C/Mendizabal s/n, 15403 Ferrol, Spain

ARTICLE INFO

Keywords:
High entropy alloys
Laser cladding
Microstructure
Wear

ABSTRACT

A non-equiatomic $Fe_{50}Mn_{30}Co_{10}Cr_{10}$ alloy was prepared by laser cladding, and the effects of boron addition on the microstructure, hardness and abrasive wear-resistance were investigated. Elemental powders were mixed using an attritor mill for 30 h and then applied by laser cladding on a stainless steel 316L substrate. The effect of boron addition (0.1, 0.66 and 5.40 at%) on the alloy microstructure was assessed using optical and electron microscopy, and the phase composition was studied using X-ray diffraction. The laser claddings were exposed to abrasive wear conditions using the dry sand/rubber wheel test. The microstructure of the laser claddings exhibited columnar dendrites formed by two crystalline structures (fcc and hcp) with the same chemical composition. The hcp structure was the result of the partial martensitic transformation of the fcc structure. Boron addition led to the formation of a eutectic phase along the interdendritic regions with a crystalline structure consistent with M_2B-type borides (M = Cr, Fe). Hardness and abrasive wear-resistance of the laser claddings were strongly influenced by boron content. When boron content was increased from 0 at% to 5.40 at% the microhardness of the material was from 291 HV to 445 HV. Similarly, the boron content improved the behaviour against abrasive wear due to the increased volume fraction of borides in the microstructure. The high content of the boride phase in the laser cladding with 5.40 at% B allowed reducing the abrasive wear rate by more than 30% when compared with the alloy without boron content.

1. Introduction

Multi-component and high-entropy alloys (HEAs) are nowadays a new class of materials with an attractive microstructure-properties-performance relationship. A wide range of properties such as high strength, ductility, hardness, fracture toughness, thermal stability at high temperature, corrosion and wear resistance, and oxidation resistance has allowed novel engineering applications in aeronautics, automotive and construction industries [1–11]. In the last decade, many HEAs have been fabricated in search of materials with outstanding strain-hardening behaviour [12–14].

Recently, Li et al. produced non-equimolar $Fe_{50}Mn_{30}Co_{10}Cr_{10}$ alloy by vacuum induction-melted and thermo-mechanical treatments [15]. In this regard, the $Fe_{80-X}Mn_XCo_{10}Cr_{10}$ (x = 45, 40, 35 and 30 at%) Fe-base alloy presented a partial athermal martensitic transformation from fcc to hcp due to a reduction of the thermal stability of the fcc phase owing to quenching from the high temperature single-phase region that led to the subsequent formation of the DP (fcc + hcp)-HEA. Additionally, the addition of interstitial elements such as carbon, can generate exceptional mechanical properties [16,17].

Specifically, the $Fe_{49.5}Mn_{30}Co_{10}Cr_{10}C_{0.5}$ alloy with $M_{23}C_6$ carbides acting as nanoparticles embedded coherently within an fcc structure, achieved improvements in the strength-ductility due to the activation of both twinning- (TWIP) and transformation- induced plasticity (TRIP) hardening mechanisms. This new alloy design has been then called TWIP-TRIP (fcc + hcp)-HEAs [16]. Similarly, when 30 ppm of boron is

* Corresponding authors at: Mechanical Engineering Department, Faculty of Mathematical and Physical Sciences, University of Chile, Beauchef 851, Santiago, Chile (J.Y. Aguilar-Hurtado). CSIRO Manufacturing, Gate 5, Normanby Road, Clayton, VIC 3168, Australia (A. Vargas-Uscategui).
E-mail addresses: jaguilarhurtado@ing.uchile.cl (J.Y. Aguilar-Hurtado), alejandro.vargas@csiro.au (A. Vargas-Uscategui).

https://doi.org/10.1016/j.apsusc.2020.146084
Received 13 November 2019; Received in revised form 19 February 2020; Accepted 12 March 2020
Available online 13 March 2020

added to equiatomic $Fe_{20}Mn_{20}Cr_{20}Co_{20}Ni_{20}$ and non-equiatomic $Fe_{40}Mn_{40}Cr_{10}Co_{10}$ alloys, an ultra-strong and ductile HEA is obtained as a consequence of the interface strengthening and grain size reduction caused by boron [17–19]. It is important to highlight that these works have been carried out with a focus on structural applications. Moreover, the $Fe_{50-x}Mn_{30}Co_{10}Cr_{10}B_x$ (x = 0, 0.3, 0.6 and 1.7 wt%) alloy system manufactured by the conventional method arc melting has shown increased hardness due to the formation of a dual-phase (fcc/hcp) matrix with M_2B-type borides (M = Cr, Fe) when boron content is increased [20,21].

In general terms, such effect of boron ranging from a strengthened solid solution and an improved grain boundary cohesion to the formation of hard boride phases shows to be promising when both mechanical properties and wear resistance are required [9,22–29]. In this sense, the HEAs with boron addition could bring a solution to industrial applications where equipment deterioration is due to abrasive wear. The problems associated with severe plastic deformation and crack formation and propagation at the surface level could be controlled by having a more resilient and tough matrix which embeds a hard boride phase into it. Therefore, the idea that adding boron to a non-equiatomic $Fe_{50}Mn_{30}Co_{10}Cr_{10}$ will have a beneficial effect on the abrasive wear resistance of this material has motivated the research work presented here.

Currently, laser cladding is one of the most relevant methods used in surface engineering. The technique allows achieving high cooling rates (10^3-10^6 Ks^{-1}) within a narrow heated zone while the dilution is lower when compared with conventional methods [30,31]. The latter has an impact on the formation of fine microstructures with non-equilibrium phases and increased solubility [31–33]. Hence, laser cladding is an attractive method to manufacture a multi-component alloy with the desired phase composition [34,35].

Here, we propose using laser cladding to produce a modified version of the new non-equiatomic $Fe_{50}Mn_{30}Co_{10}Cr_{10}$ alloy with different additions of boron (between 0 at% and 5.40 at%). The effect of boron addition on the microstructure was assessed using optical and electron microscopy, and the phase composition was studied using X-ray diffraction. The laser claddings were exposed to abrasive wear conditions and attention was giving to the effect of boron on the abrasive wear resistance. The main experimental findings are discussed, and indications about the potential of the non-equiatomic alloy for surface engineering applications are given.

2. Experimental details

2.1. Preparation of alloy powders

Table 1 shows the chemical composition of the powders used to manufacture the non-equiatomic alloys. Elemental powders of Fe (99 wt%), Mn (99.5 wt%), Co (99.9 wt%), Cr (99 wt%) and B (92.1 wt %) were mixed following the nominal composition provided in previous work [21]. The particle size for each powder used in the fabrication of the coatings is presented in Table S1. The powder mixture was processed for 30 h by mechanical alloying (MA) using an attritor mill at a speed of 425 rpm and a 10:1 ball-to-powder mass ratio under an argon atmosphere. This method showed to be adequate to homogenise the chemical composition and thus avoiding composition variations during the laser cladding process. The jar, balls and impeller were made of stainless steel AISI SAE 304. No lubricants or additives were used to avoid contamination [36]. A multimodal particle size distribution was generated in all samples milled for 30 hr due to the difference in the particle size of the precursor elements of the alloy system proposed. In this sense, the powders characterisation by laser granulometry allowed to establish that the 90% of the mechanically milled powders did not exceed 18.22 μm in MA-B0, 25.36 μm in MA-B3, 24.58 μm in MA-B5 and 37.92 μm in MA-B10 (see Fig. S1). ICP-OES (Inductively coupled plasma - optical emission spectrometry) was used to measure the chemical composition of the powders. The powders were pressed at an equivalent pressure of 35.05 MPa to form a powder compact with a thickness of 1 mm before the laser cladding process.

Table 1
Chemical composition of the powders used for the laser cladding process (in at %).

Powder	Fe	Mn	Co	Cr	B
MA-B0	48.63	31.13	10.41	9.83	0.00
MA-B3	45.95	30.87	10.37	9.74	3.06
MA-B5	43.86	30.81	10.34	9.95	5.03
MA-B10	39.89	30.34	10.50	9.97	9.30

2.2. Laser cladding process parameters

A 2.2 kW continuous-wave diode-pumped Nd-YAG laser (Rofin DY022) mounted on a robotic arm, with a wavelength of 1064 nm was used to manufacture the claddings. High-purity argon gas was used as a shielding gas to prevent oxidation. Laser parameters, namely laser power, scanning velocity and diameter beam, were optimised for each of the prepared powders in order to obtain a fully melted and dense material (lack of pore, voids, cracks, etcetera) upon deposition. Table 2 shows the optimised process conditions that were used to obtain uniform samples labelled as LCA-B0, LCA-B3, LCA-B5 and LCA-B10. A conventional stainless steel 316L was used as substrate ($72.5 \times 23.5 \times 9.5$ mm^3), and the compacted powder was placed on top of it after the substrate was cleaned with acetone and dried. By the action of the laser beam, the powders were melted and rapidly solidified in multiple tracks to produce a cladding layer of about 0.3 mm thickness. This process was repeated by overlaying multiple layers until an almost uniform coating thickness of 2.5 mm was obtained in all alloys proposed. The appearance of the laser claddings can be seen in Fig. S2 (supplementary material).

2.3. Materials characterisation

The chemical composition of the claddings was analysed using glow-discharge optical emission spectrometry (GD-OES, Spectrum GDA 750 HR), while the substrate was analysed using inductively coupled plasma optical emission spectrometry (ICP-OES, Varian 730-ES axial). The GD-OES analysis was performed on the top surface of the laser cladding material.

After producing the claddings, samples were extracted and prepared using standard metallographic procedures. Specimens prepared along the cross-sections of the laser cladding alloys were polished and observed using optical microscopy (OM) and scanning electron microscopy (SEM, FEI Quanta 250) fitted with an Oxford Instruments Energy Dispersive X-Ray Spectrometer (EDS), at an operating voltage of 20 kV. Both microstructure and a chemical composition maps were studied at the micron scale using SEM-EDS. The samples were chemically etched using Nital (10%) and aqua Regia when necessary.

Table 2
Processing parameters used for the laser cladding process.

Cladding	Laser power (J/s)	Scanning velocity (mm/s)	Beam diameter (mm)	Specific energy (J/mm^2)	Heat input (J/mm)
LCA-B0	1200	10	2	60	120
LCA-B3	1000	5	2	100	200
LCA-B5	1000	5	2	100	200
LCA-B10	1000	5	2	100	200

X-ray diffraction (XRD) was used to characterise the phase constitution and crystalline structure of the coatings. A Bruker D8 Advance A25 X-ray diffractometer operating under CuKα (λ = 1.542 Å) radiation (40 kV, 40 mA) equipped with a Lynx Eye XE-T detector was employed to obtain the XRD patterns. The samples were scanned over the 2θ range 5° to 130° with a step size of 0.02° and a count time of 1.6 s per step and were spun at 15 rpm during data collection. Rietveld analyses were performed on the data using the Bruker TOPAS™ V5 program to quantify the phases. Background signal was described using a combination of Chebyshev polynomial linear interpolation function and 1/x function. Cell parameters, vertical sample displacement, the full width at half maximum, preferred orientation and peak scale factors were all refined. During phase refinement, constraints were placed upon sample composition based on the supplied chemistry.

Additionally, the maximum enthalpy for intermetallic/multiphase formation (ΔH_{max}), and the solid solution forming ability (Φ) were determinate using the simulation platform alloyASAP [37]. This new approach is a method to predict the formation and stability of single phase of HEAs proposed recently by King et al. [38].

2.4. Mechanical testing

The micro-hardness was tested by a microhardness tester (Struer Duramin ± 1/2) with a load of 1000 g and loading time of 15 s. Measurements were done on the cross-section of each sample produced by laser cladding and multiple indents separated by 150 μm were done from the top surface through the thickness of the cladding. The average values and their standard deviation were calculated from 20 measurements.

2.5. Wear test

Samples for wear tests were cut with a dimension of 76 × 24 × 9.5 mm^3 and were machined to obtain a flat surface. Abrasion tests were performed in an abrasion testing machine following the procedure E described in the ASTM standard G65. The total test time was 5.45 min and a load of 130 N was applied while the rubber wheel rotated at a speed of 186.6 rpm [39]. After the abrasion test, the samples were thoroughly cleaned with acetone in an ultrasonic bath for 3 min before weighing in a balance with a resolution of 0.0001 g (Radwag AS 82/220.R2). Mass loss was converted to volume loss using the density of each non-equiatomic alloy which was measured by using the Archimedes' principle. The wear test was repeated three times, and the reported values represent an average of the measurements.

3. Results and discussion

3.1. Chemical composition

As shown in Table 2, input laser specific energy had to be set to higher values in the case of the boron-containing powders, as they showed less absorptance to laser radiation. A plausible explanation for this difference is the known boron ability to provide self-fluxing characteristics to conventional Fe, Co and Ni-based alloy powders used for coating purposes. Boron acts as a fluxing agent, which promotes wetting by reducing the presence of oxides in the melt pool and controlling the surface tension of its thin surface film. As a consequence this surface appears more metallic and reflective, thus diminishing the absorption rate of laser radiation [40]. The afore mentioned also could explain the boron losses reported in Table 2.

Table 3 shows the chemical composition of the coatings produced by laser cladding and the composition of the substrate before the process measured by GD-OES. The content of the alloying elements in the laser cladding material notably changed when compared to the composition of the starting powders. Even though it was not observed a systematic behaviour, boron addition alters the composition of the alloy and thus enhanced the addition of Mn in the alloy, while Fe content tends to decrease slightly. In particular, Mn has a high vapour pressure and tendency to oxidation, which makes chemical composition control challenging in the laser cladding process [41,42]. However, boron addition reduces the melting temperature of the alloy, which in turns avoids the vaporisation of Mn [43]. Similar behaviour was observed when these alloys were produced by arc-melting [21]. Although dilution is known to be low in laser cladding when compared to other techniques such as welding [44], a low Ni content introduced from the substrate was detected in the laser claddings.

Due to the use of elemental powders in the preparation of the powder mixtures, the effects of oxidation and slag formation on the metallic loss cannot be ignored and therefore the variations noticed in the chemical composition of the laser claddings. In addition to this, it is essential to consider the particle size effect on the laser cladding process. In this sense, Tanigawa et al. suggested that a particle size of 30 μm is the minima to obtain an acceptable coating [45]. However, in this case, the particle size of the powders mixture did not exceed (D_{90}) between 18.22 and 37.92 μm, being the smaller particles more prone to absorb the laser energy more rapidly increasing the temperature up to a point where oxidation and volatilisation are favourable instead of maintaining a stable melt pool. Oxidation can be particularly important when considering that Fe, Mn, Co, Cr and B can react with the trapped air in the pre-deposited powders [29,46].

3.2. Analysis of the microstructure

Fig. 1 shows the microstructure of the as-deposited laser claddings over the cross-section of the samples. The images show the interface between the cladding and the substrate as a nearly straight line, and where the cladding is in the top section and the substrate is in the bottom part of the image. Some pores were observed in the cross-section of the material along with pitting due to the use of aqua Regia as a reagent for chemical etching. The boron free alloy (LCA-B0) showed a typical columnar dendritic microstructure free of segregation (see Fig. 1a). The laser claddings LCA-B3 and LCA-B5 shown a columnar dendritic microstructure that grew perpendicular from the interface as can be seen in Fig. 1b and c, respectively. A very narrow region along the interdendritic boundary due to the segregation of a eutectic phase was also seen in the laser claddings LCA-B3 and LCA-B5. An evident change in the microstructure can be seen in the alloy LCA-B10, where the proportion of the eutectic phase between the dendrites was increased (see Fig. 1d). The presence of the eutectic phase is directly related to the increased content of B in this alloy composition.

Perpendicular cracks along the direction of the solidification front were only observed in the laser cladding LCA-B3, and no cracks in the base material were evidenced, as shown in Fig. S3. The presence of these interdendritic cracks is attributed to the segregation of the eutectic boron-rich phase and the rapid cooling rate experienced during laser cladding [47]. The latter proves to be true when considering that it has been reported that 50 ppm of B can be regarded as a critical level of addition to this type of alloys because above this level the formation of brittle compounds makes the grain boundary weak [17]. Interestingly, no signs of crack formation were observed in the laser claddings LCA-B5 and LCA-B10 where boron content was well above this doping critical level. In such cases, the absence of cracks can be explained considering that the amount of eutectic phase increases up to a level where it forms a continuous path between the dendrites allowing a better load transfer between the phases when thermal stress is produced during the cooling regime.

Fig. 2 shows the most significant features of the microstructure found after further SEM inspection of the laser claddings. The

Table 3
Chemical composition of the coatings produced by laser cladding (in at%) measured by GD-OES. The number in parentheses indicates the relative change compared to the chemical composition shown in Table 1.

Cladding	Fe		Mn		Co		Cr		B		Ni
LCA-B0	63.33	(+30%)	17.31	(−44%)	12.02	(+15%)	6.89	(−30%)	0.00	(0.00)	0.45
LCA-B3	54.24	(+18%)	25.64	(−17%)	11.08	(+7%)	8.70	(−11%)	0.10	(−97%)	0.25
LCA-B5	43.06	(−7%)	37.94	(+23%)	8.33	(−19%)	9.78	(−2%)	0.66	(−87%)	0.22
LCA-B10	36.18	(−9%)	42.04	(+39%)	8.02	(−24%)	8.28	(−17%)	5.40	(−42%)	0.08
Substrate [a]	69.19		1.44		0.18		18.32		0.00		9.74

[a] The chemical composition of the substrate includes 1.13 at%-Mo content.

microstructure of the LCA-B0 (Fig. 2a) showed the characteristic morphology of a dendritic structure with a fine blocks-like or sheaves-like crisscrossed morphology randomly distributed across the dendrites, that are characteristic of ε-hcp-martensite [48–50] and the presence of annealed twins is related with the deformation resultant from the thermal contraction of the material [51,52]. Fig. 2b shows the microstructure of the LCA-B3 cladding. The microstructure is composed of a dendritic structure and a very thin discontinuous segregation in the interdendritic regions. Also, a morphology of "striations" formed within the dendritic zones was observed, which is similar to the athermal martensitic transformation from fcc to hcp in Co-based alloys [53,54]. These striations were barely noticed in LCA-5 and LCA-B10 coatings. Boron addition causes the segregation of a eutectic phase in the interdendritic spaces, and the SEM images confirm the previous findings described from the optical microscopy analysis. The width of the interdendritic spacing varies from ~1.36 ± 0.29 μm in LCA-B3 to ~2.25 ± 0.61 μm in LCA-B5 and ~4.62 ± 2.94 μm in LCA-B10. Overall, the microstructural features of the alloy system obtained by laser cladding were similar to those reported for similar compositions but produced using arc-melting [21].

The variations of the chemical composition on the cross-section were studied using EDS elemental mapping, and the maps of the main constituents are shown in Fig. 3. The laser cladding without boron addition (LCA-B0) did not show a variation in the distribution of the alloying elements inside or between the dendrites which confirms the formation of a chemically homogeneous alloy with all the elements in solid solution. As expected, the EDS maps of the laser claddings with boron addition (i.e. LCA-B3, LCA-B5, and LCA-B10) showed the segregation of one of alloying elements within the eutectic phase. Although EDS has some sensitivity limitations, the maps show enrichment in the chromium content in the eutectic phase, which increases with boron addition in the laser cladding. However, Mn and Co did not show the same contribution in the eutectic region as they did in the matrix. The Fe behaves alike, and the content is lower in the eutectic phase than inside the dendrites. As previously described, some nickel content was introduced in the laser cladding after the process, and the EDS maps showed a homogeneous distribution (Fig. S4 of the Supplementary material).

3.3. XRD analysis

Fig. 4 shows the XRD patterns of the multi-component alloy with different additions of boron produced by laser cladding. Based on what is observed on the XRD pattern of the laser cladding without boron addition (LCA-B0), the alloy system formed two different crystalline structures, fcc and hcp. Therefore, it is suggested that this hcp phase identified by XRD is produced by an athermal martensitic transformation like the one reported by Li et al. [15]. The homogeneous chemical distribution observed in Fig. 3a confirmed that both fcc and hcp phases have the same chemical composition, and the hcp phase was likely

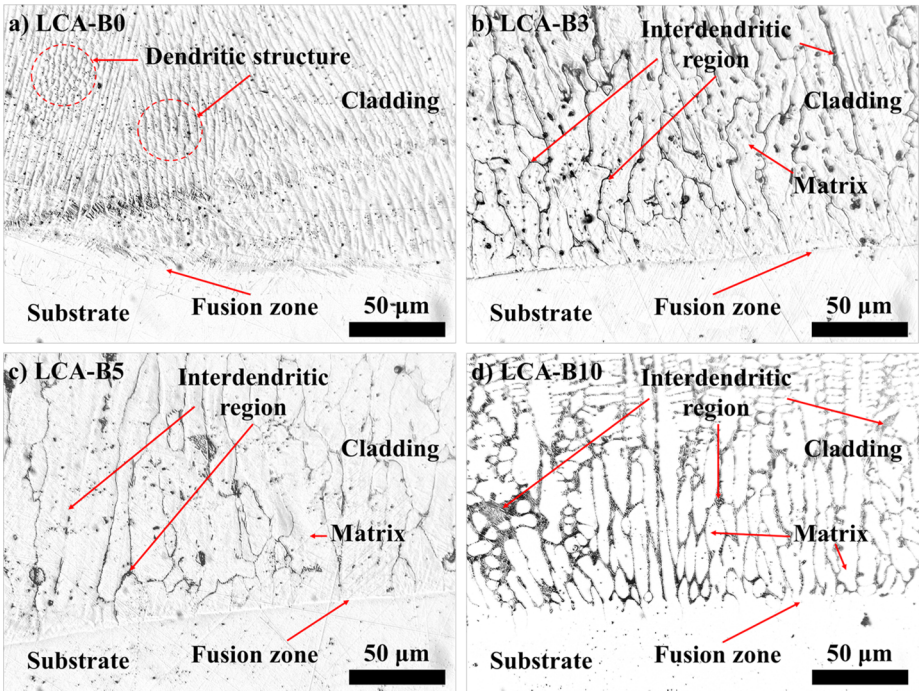

Fig. 1. Optical micrograph showing the microstructure in the cross-section of the laser claddings. (a) LCA-B0, (b) LCA-B3, (c) LCA-B5, and (d) LCA-B10.

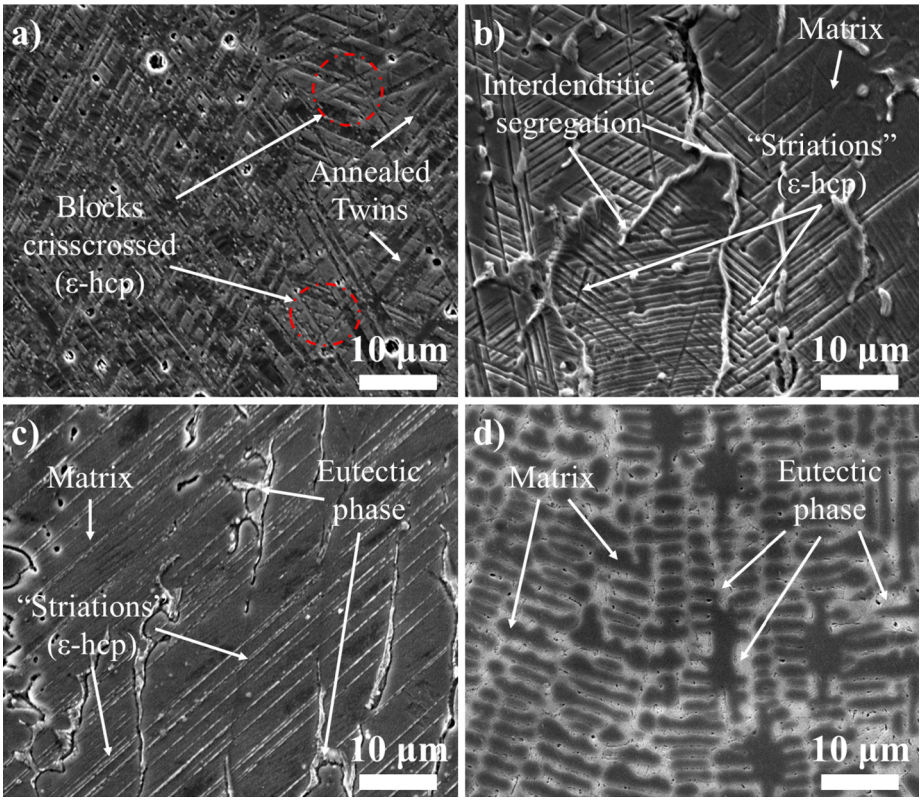

Fig. 2. SEM micrographs of (a) LCA-B0, (b) LCA-B3, (c) LCA-B5, and (d) LCA-B10.

formed by a martensitic-like partial transformation of the fcc during rapid solidification. Also, it is important to mention that a bcc phase was only detected in the laser cladding LCA-B0. This phase has been found in the equiatomic FeMnCoCr alloy together with the fcc phase. Bracq et al. [55] also demonstrated that only the hcp phase was obtained when Co concentration exceeded 80 at. %. According to this, the bcc phase in this work could be considered as non-equilibrium phase formed due to the effect of high mixing entropy, the advantageous rapid solidification observed in laser processing [56,57], and the increase of laser powder used in the LCA-B0 reported in Table 2. Finally, it is important to highlight that the Co has a stabilising effect on the fcc phase, while Cr stabilises the bcc [19].

Except for the peak related to the bcc structure, the peaks that correspond to the fcc and hcp crystalline structure were present in the laser claddings with boron addition. Interestingly, the intensity of the peak located at $2\theta = 50.79^{\circ}$ associated with the crystallographic planes {2 0 0} in the fcc structure increased with boron addition (i.e. LCA-B3, LCA-B5, and LCA-B10). However, the most critical effect observed in the XRD patterns was the presence of the orthorhombic $(Cr, Fe)_2B$ boride due to the presence of boron in the alloy system. This result confirms the findings of the microstructural analysis and allows establishing that the eutectic phase segregated in the interdendritic spaces is $(Cr, Fe)_2B$ boride. The results are also in agreement with the findings reported by us using arc melting [21]. Additionally, some weak peaks corresponding to MnO were also detected in some of the samples. Based on the microstructural analysis, this oxidation was due to the interaction between the samples and the air.

Fig. 5 shows the results of the quantification of the relative phase composition of the laser claddings done by the Rietveld refinement technique. The analysis showed that the content of the hcp structure was always higher than the content of the fcc structure for the explored compositions, which confirm the presence of an athermal martensitic transformation. The laser cladding without boron content (i.e. LCA-B0) exhibited the highest content of the hcp structure (85%), while at the same time had the lowest content of the fcc structure (1.2%). This result shows that the cooling rate also plays an essential role on the martensitic transformation of this alloy system, especially when comparing to results obtained from arc melting [21] and a thermo-mechanically homogenised alloy [15] where the content of the hcp phase was 79% and 28%, respectively. Also, the hcp content is related to the introduction of stacking faults through the glide of partial dislocations or by the overlapping of these [12,49]. In this sense, the stacking fault energy (SFE) was estimated using an empirical formula proposed by Schramm and Reed which related this energy with the chemical composition [58,59]. The results suggest that in LCA-B0, where the Mn content is lower than in LCA-B3 to LCA-B5 alloys, the SFE is < 20 mJ/m^2 which favor the stacking faults formation and, therefore, the increase in the amount of the hcp phase [49,50]. When boron is added and the Mn content increases, the SFE raises along with a decrease in M_s temperature hindering the hcp formation. Due to the boron segregation in the interdendritic regions, the stacking faults could not extend indefinitely as consequence of the local variation in fcc_{SF} (stacking faults in fcc structure) with the boron content of these crystalline defects [54]. However, although there was a decrease in hcp phase when boron was added, the laser rapid solidification experience during laser processing introduced a high density of fault defects including twins and stacking faults which contributed in the hcp formation [54]. Furthermore, the hcp/fcc ratio showed a slight increment from 1.6 to 2.0 among the samples with boron addition (i.e. LCA-B3, LCA-B5, and LCA-B10). The variation of this ratio is a consequence of the presence of the boride phase, which increased with boron content, and the intrinsic effect of the metallic losses of the gamma (fcc) stabiliser elements [19]. Although the boride phase was detected during the microstructural analysis, the Rietveld refinement did not allow quantifying its content in

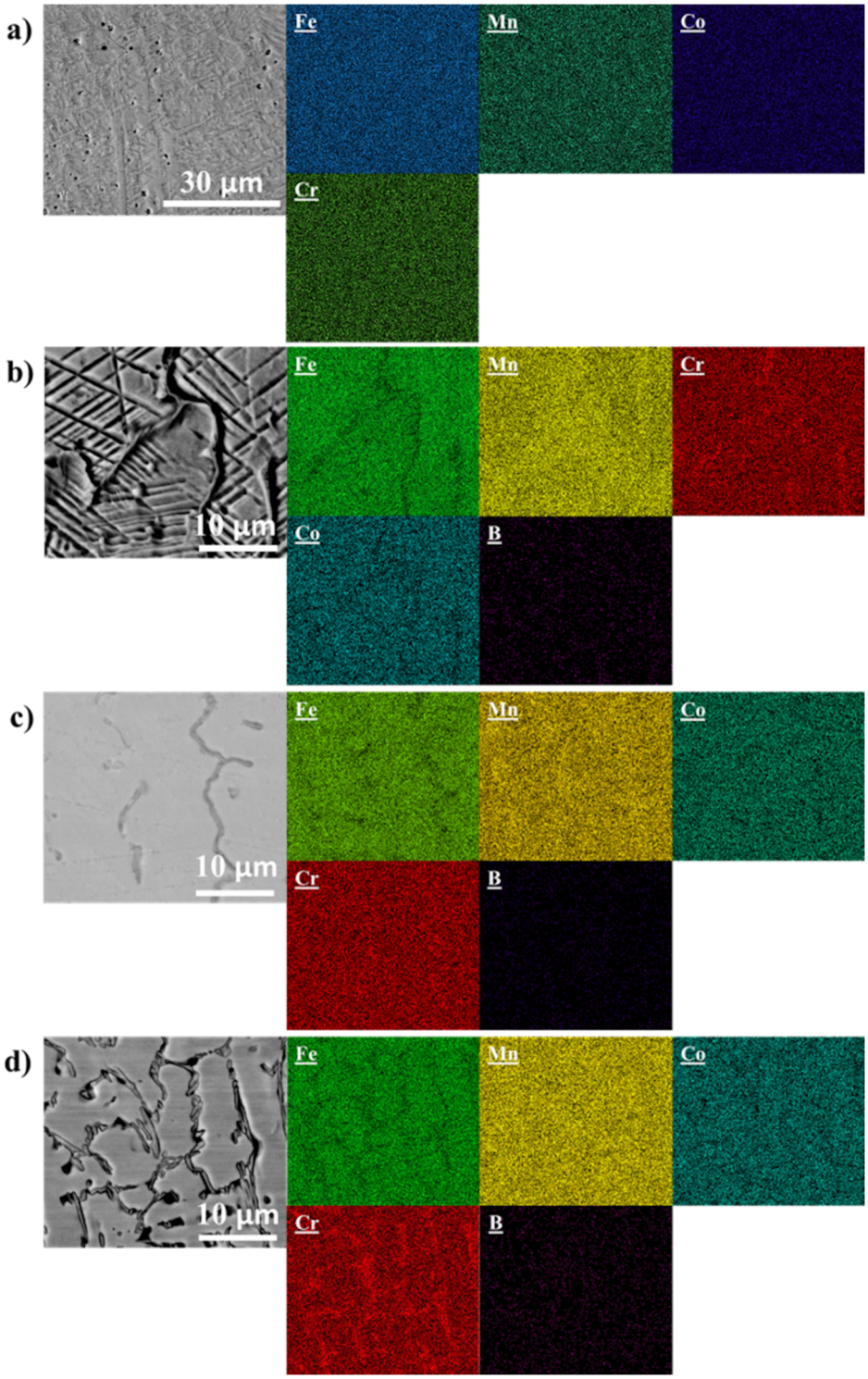

Fig. 3. EDS elemental mapping of the laser claddings (a) LCA-B0, (b) LCA-B3, (c) LCA-B5, and (d) LCA-B10.

the laser cladding LCA-B3. In contrast, the laser claddings LCA-B5 and LCA-B10 showed an increment from 3% to 9% in the content of the boride phase. The formation of M_2B-type borides Cr-rich is due to the strong interaction energy of the pairs Fe-B (−26 kJ/mol) and Fe-Cr (-31 kJ/mol) which facilities the segregation of these intermetallics [60].

Table 4 shows the lattice parameters for the identified phases in the laser claddings (except for MnO). From this data, it can be noted that the lattice parameter of the fcc phase and the c parameter of the hcp phase slightly increased with boron content. This behaviour can be explained considering that fcc phase have two interstitial sites in the formation of solid solution, one tetrahedral and another octahedral site. Under ideal conditions and supposing that the atoms in the crystalline structure are spheres, the radius of the tetrahedral cavity is 0.225 r, while the octahedral is 0.414 r, where r is the radius of the atom that could occupy these cavities [46]. Taking as reference the crystalline

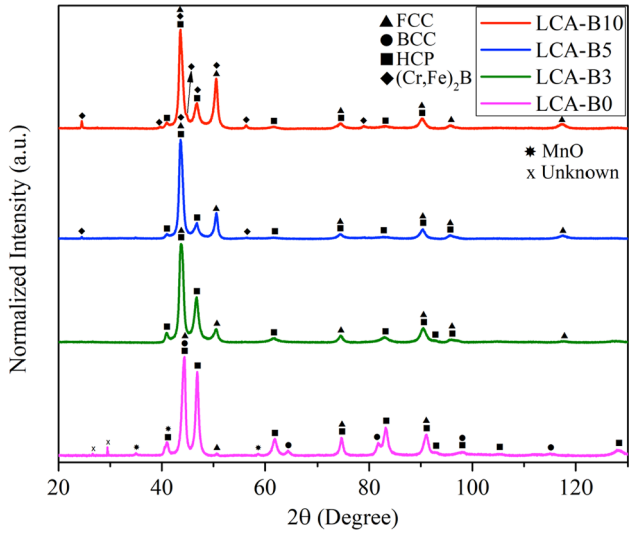

Fig. 4. XRD patterns of the LCA-B0, LCA-B3, LCA-B5 and LCA-B10 specimens obtained by laser cladding.

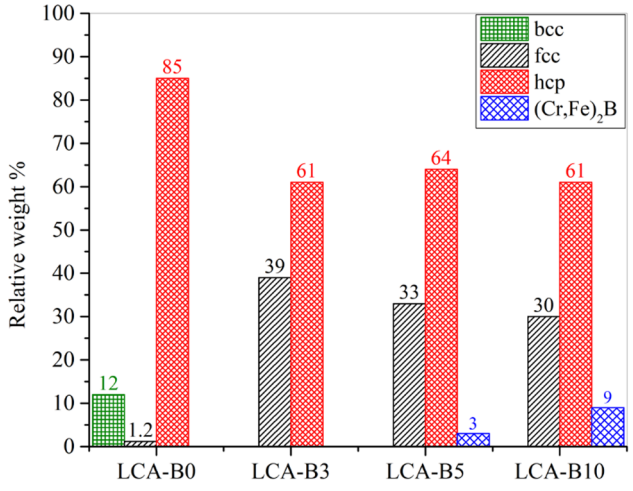

Fig. 5. Relative phase composition from Rietveld refinement with XRD data for laser cladding samples LCA-B0, LCA-B3, LCA-B5, and LCA-B10. It should be noted that the balance of the quantification matches the MnO content.

Table 4
Lattice parameters of the identified phases in the laser claddings (values in Å).

Cladding	bcc	fcc	hcp		$(Cr, Fe)_2B$		
	A	a	a = b	c	a	b	c
LCA-B0	2.884	3.594	2.540	4.097	–	–	–
LCA-B3	–	3.597	2.539	4.117	–	–	–
LCA-B5	–	3.604	2.542	4.130	14.551	7.282	4.164
LCA-B10	–	3.607	2.540	4.131	14.523	7.292	4.159

radii of Fe (0.069 nm), Mn (0.081 nm), Co (0.054 nm), Cr (0.076 nm) and B (0.025 nm), the average crystalline radius of the FeMnCoCr system would be approximate 0.070 nm. Those mentioned above indicates that boron could only be hosted in the octahedral cavity, whic radius is 0.029 nm. This configuration would explain the increase in the parameter *a* of the fcc phase. In contrast, the *c/a* ratio of the hcp phase would be related to solute entrapment during the rapid solidification experienced in laser processing which increased the solubility of the

Table 5
Calculated thermodynamic parameters $Fe_{50-X}Mn_{30}Co_{10}Cr_{10}B_X$ (x = 0, 0.02, 0.13 and 1.10 wt%) multi-component alloys produced by laser cladding.

Alloy	ΔH_{max} (kJ/mol)	ΔS_{conf} (R)	ΔS_{mix} (J/°Kmol)	δ_r	VEC	Φ
LCA-B0	−14.87	1.72	14.33	3.22	7.42	1.17
LCA-B3	−95.63	1.35	11.20	3.85	7.35	0.19
LCA-B5	−103.29	1.00	8.30	5.78	7.23	0.17
LCA-B10	−159.62	1.22	10.17	9.38	7.01	0.13

boron in the phases of the matrix (fcc + hcp) [25,49]. Furthermore, the boron content in the orthorhombic phase M_2B (only 9 wt% in this compound) is low compared to the total boron amount in the coatings (see boron content in Table 1), suggesting that boron formed solid solution phases with the other elements in the matrix.

A detailed review of the diffractograms (see Figs. S5 and S6 of the supplementary material) allowed to establish that the position of six peaks shifted towards the left as a consequence of an increase in the boron content. This behavior is closely related to the lattice parameter increasing along with lattice distortion when boron is added [29].

3.4. Thermodynamic prediction of the $Fe_{50-X}Mn_{30}Co_{10}Cr_{10}B_X$ (x = 0, 0.1, 0.66 and 5.40 at%) alloy system.

The same methodology to study the thermodynamic prediction of the formation and stability of phases formed through of arc-melting was used in the coatings produced by laser cladding [21,38]. Table 5 shows the calculated thermodynamic parameters of the laser claddings LCA-B0, LCA-B3, LCA-B5, and LCA-B10, considering the content of Ni reported in Table 2. Based on the configurational entropy (ΔS_{conf}) [61,62], the LCA-B0 can be considered as a metastable high entropy alloy due to ΔS_{conf} greater than 1.6R. In this case, the Ni content did not have a considerable effect on thermodynamical parameters of the $Fe_{50-X}Mn_{30}Co_{10}Cr_{10}B_X$ systems, suggesting that Ni did not tend to segregate, and on the opposite, it formed a solid solution until it reached the thermodynamic equilibrium.

On the other hand, the laser claddings LCA-B3, LCA-B5 and LCA-B10 should be addressed as medium-entropy alloys (MEAs) because the configurational entropy varies between 1R and 1.5R [62]. According to the literature, a single-phase HEA in solid solution occurs when $\Phi \geq 1$, $\sim 1.2 \leq \delta_r \leq 6.6$ and -15 kJ/mol $\leq \Delta H_{max} \leq 5$ kJ/mol, while multiphase/intermetallic HEA happen when $\Phi < 1$, $\sim 1 \leq \delta_r \leq \sim 13.5$ and $\sim$-90 kJ/mol $\leq \Delta H_{max} \leq \sim$25 kJ/mol. In this sense, the thermodynamic prediction shown in Table 5 indicates that the values of Φ, ΔH_{max} and δ_r satisfy the conditions for phases formation in a solid solution for the LCA-B0 cladding. While in the boron-containing claddings, ΔH_{max} does not meet the requirements for a multiphase HEA owing to the interaction between boron and other elements present into the multi-component alloys [38]. According to Guo et al. [63], both fcc and bcc phases are stable when 6.78 ≤ VEC ≤ 8.0 and that is a condition that is satisfied by all the produced laser cladding compositions. In the same direction, the thermodynamical parameter VEC and δ_r predicted in Table 5 did not satisfy the condition for a single hcp phase formation. In the prediction of the hcp simple-phase solid solution formation, VEC ~3, while the difference in atomic radii (δ_r) is ≤ 3% when HEAs including rare-earths elements [33]. It has only been reported transition metals HEAs with Re and Ru, which parameter VEC = 8 and δ_r ranged between 3 and 4% [64]. However, it should be noted that the presence of the hcp phase in the laser claddings is a consequence of a non-equilibrium process in which the martensitic transformation of the fcc phase took place.

Due to the presence of Ni in the alloy system, ΔH_{max} and phi (Φ) parameters were calculated considering a Ni-free (i.e. the content of Ni

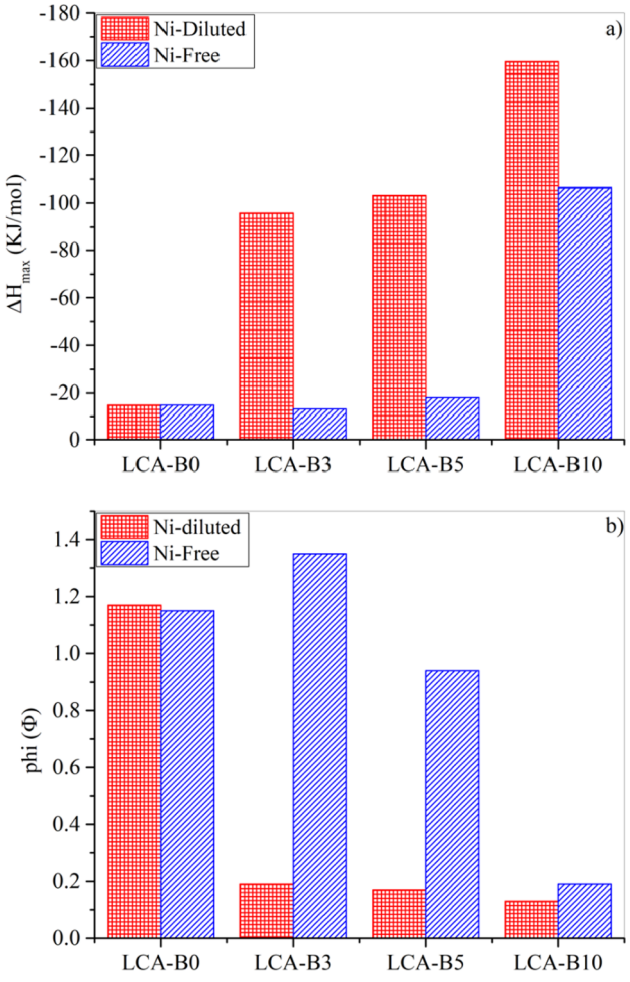

Fig 6. The values of ΔH_{max} and phi (Φ) for the laser claddings considering a Ni-free and Ni-diluted condition.

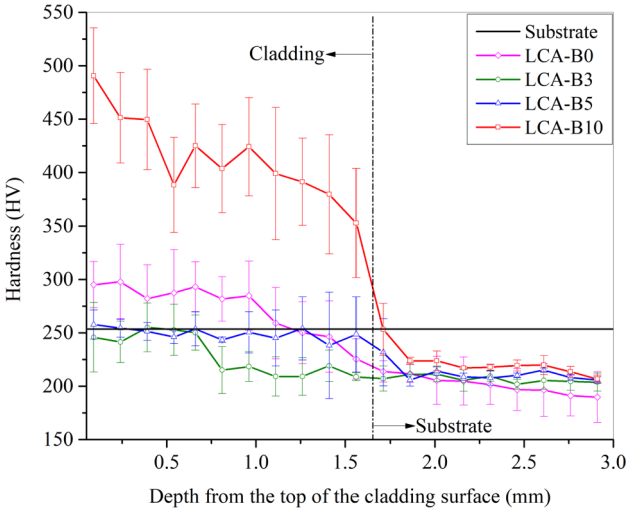

Fig. 7. Vickers hardness cross-section profiles for the laser claddings LCA-B0, LCA-B3, LCA-B5 and LCA-B10 on AISI 316L steel. The solid line corresponds to the hardness of the substrate before the laser cladding process (253.13 ± 11.31HV).

is 0 wt%) and Ni-diluted (i.e. all the Ni forms solid solution) condition with the purpose to study the effect of the Ni from of a point view thermodynamic and the values were plotted in Fig. 6. The comparison shows that the presence of Ni in the alloy system tends to reduce the values of ΔH_{max} and Φ significantly. Comparing these results with microstructure features, specifically, in LCA-B3 and LCA-B5 specimens, the solid solution phase formation decreases with Ni dilution. According to the rule for phase formation in HEAs, an increasing number of elements means that configuration entropy rises; however, the addition of more elements increases much more the binary interaction compared to the entropy [65]. The latter means that Ni could promote a decreased solubility of boron in the matrix of the alloy and facilitate and thus facilitate the interaction between the pairs Fe-B and Cr-B to form borides [65–67]. A similar phenomenon has been observed in thermodynamic studies on equiatomic HEAs with carbon additions as an interstitial element [67].

3.5. Mechanical properties

Fig. 7 shows the cross-sectional Vickers hardness of the laser claddings taken from the top of the surface. For the sake of comparison, it should be noticed that the hardness of the substrate decreased after the laser cladding process due to the softening induced by the thermal cycle. In this sense, the data shows that the hardness of the laser claddings material is higher than the hardness of the substrate after the process. It can be observed that the laser cladding LCA-B0 stands above the laser claddings LCA-B3 and LCA-B5. In this respect, it should be recalled that different process parameters were applied to produce boron-containing claddings to overcome their difference in laser absorption. It is known that laser processing conditions determine the thermal cycles that the deposited material undergo and so the resulting microstructure. Higher scanning speeds translate in faster solidification rates, usually giving rise to finer microstructures, lower segregation and increased hardness. However, upon successive material deposition and corresponding reheating cycles, this feature tends to be mitigated, yielding a more softened structure. Therefore, even if the enhanced hardness of the LCA-B0 is possibly due to the higher proportion of the hcp phase in its microstructure, the effect of the higher laser processing speed cannot completely be discarded.

Although the presence of the boride phase in the laser cladding LCA-B5 is about 3 wt%, the results of the microhardness analysis indicate that the abundance of the hcp structure in the matrix could have a more significant effect on the hardness than the borides presence up to that level. However, the decrease in microhardness of alloys with boron contents intermediate (LCA-B3, LCA-B5), suggests that the hardening mechanism by solid solution was affected by the decay of Fe and Cr in the matrix due to the borides phase formation and the presence of the fcc phase.

On the other hand, the dispersion and decrease of hardness observed in Fig. 7 from the surface of the deposit toward the substrate, was attributed to microstructural heterogeneity and variations in dendritic spacing. According to a detailed analysis of the microstructure in LCA-B0 cladding, it was established that dendritic spacing ranged between 3.03 and 6.21 μm from the surface of the coating to the substrate, while in the LCA-B3 cladding, the spacing of the dendrites varied from 5.72 to 12.99 μm, with a microstructure predominantly columnar. This spacing suggests that both the microstructure and the formation of the fcc phase in LCA-B3 had a significant effect on the decrease in hardness reported in Fig. 7. Mainly, in the LCAB-5 specimen, a significant variation of the microstructure was observed as a consequence of boron addition. In this case, the areas closest to the surface of the coating showed a dendritic microstructure with secondary dendrites which dendritic spacing was ~4.72 μm on average. In contrast, in the intermediate zones and near the interface cladding/substrate, the dendritic

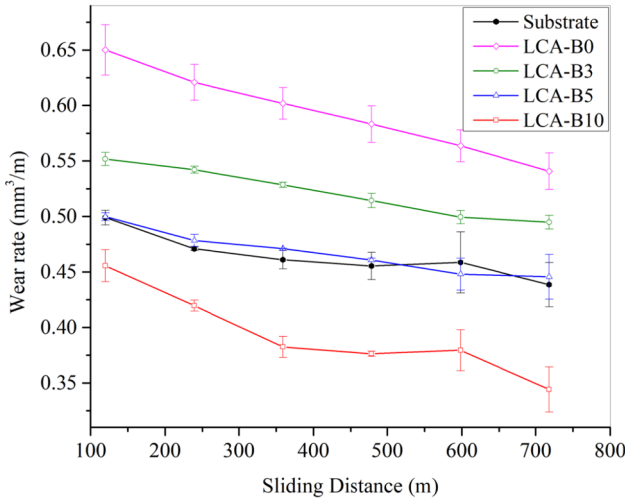

Fig. 8. Wear rate as a function of sliding distance.

spacing was 12.24 and 11.76 μm on average, respectively. Similar features were observed in LCA-B10. However, dendritic spacing ranged between 2.74 and 7.57 μm and increased towards the cladding/substrate interface. Then, the high dispersion in the hardness values for LCA-B10 up to a depth of 1.6 mm can be explained based on the dendritic spaces, which ultimately represent the extension of richer zones in the harder eutectic phase.

Finally, the laser cladding LCA-B10 which had 9 wt% of the boride phase showed a significantly increased hardness, and the value is about two times the value hardness of the substrate and about 1.5 times the hardness of the laser cladding LCA-B0. In this case, the increased hardness of the laser cladding is directly related to the increased amount of the boride phase in the microstructure. Similar values of hardness have been reported in analogues alloys produced by arc-melting and other alloying systems [21,60].

3.6. Abrasive wear resistance

The behaviour of the laser claddings against abrasive wear was evaluated using the dry sand/rubber wheel test (ASTM G65). Fig. 8 shows the wear rate as a function of the sliding distance for the specimens produced by laser cladding. As a matter of reference, the figure also shows similar data for the bare substrate. All the samples exhibited a similar tendency, i.e. the wear rate decreased with the increase in the sliding distance. This behaviour indicates that a slight surface hardening took place during the test and therefore, less material was removed due to a three-body abrasive condition [68]. The presence of the boride phase due to the boron content significantly reduces the wear rate among the laser claddings. In this sense, the abrasive wear rate diminished correspondingly when the boron content increased in the laser cladding material.

Based on the behaviour against wear tested in Fig. 8, the reduced wear performance found in LCA-B0 cladding was mainly attributed to the hcp suffered a plastic deformation of the basal planes, which favoured a high wear loss [69]. As boron was added to lead the formation of a boride phase that increased the hardness of the material, the overall significant plastic deformation should be reduced and thus the wear rate. In this context, the boron addition contributed to the reduction in wear rate observed in LCA-B3 and LCA-B5 claddings when compared to the LCA-B0. Considering the increased proportion of the fcc phase in these alloys, the amount of work hardening with the martensitic transformation and the presence of the eutectic phase will be responsible for such a reduction in wear rate. Overall, the observed effect became more noticeable in the LCA-B10 cladding in which case the lowest wear rate was observed [69,70].

When taking the laser cladding LCA-B0 as a reference, the wear rate decreased by 13%, 22% and 35% for the samples LCA-B3, LCA-B5, and LCA-B10, respectively. Thus, the sample with the highest boron content (i.e. LCA-10) showed a significant wear resistance that even outperformed the behaviour of the bare AISI 316L substrate. The results have shown that the boride eutectic phase has a positive effect on the abrasive wear mechanism by increasing the hardness of the material and protecting the matrix, thus reducing the wear rate. However, the microstructural refinement and a possible work-hardening along with phase transformation could also produce a secondary effect on wear resistance of the coating, especially, in LCA-B10.

Fig. 9a shows the worn surface morphology of the bare substrate after the wear testing. The worn surface of the substrate showed evidence of deep grooves and intense plastic deformation due to the abrasive condition. The main wear mechanisms observed in the substrate were micro-ploughing with wedge formation and micro-cutting. The adjacent material formed around the furrows is then removed, contributing to material loss because of the severe plastic deformation produced by the relative motion of the sand particles. Backscattered-electron images allowed detecting the presence of silica on the surface.

Fig. 9a2-a5 shows representative micrographs for the laser cladding material after the wear test. The images show the formation of deep grooves and significant plastic deformation along the furrows, forming a lip-shape [71]. Micro-ploughing and micro-cutting were detected on the worn surfaces. Due to intense plastic deformation, the indentation produced by sand particles generates wedge and small fracture-free lips that are then removed by the wear process. Overall, the combination of micro-cutting and micro-ploughing was more pronounced on the laser claddings than in the substrate material. However, the laser cladding LCA-B10 (Fig. 9e) showed that micro-ploughing was more evident for this material than in the others.

4. Conclusions

The effect of boron on the microstructure, mechanical properties and abrasive wear resistance of non-equiatomic $Fe_{50}Mn_{30}Co_{10}Cr_{10}$ produced by laser cladding were investigated. The metallic loss of some of the alloying elements was detected due to the adverse effects of oxidation and slag formation during the laser cladding process. Columnar dendrites were found to be a typical microstructure of the laser claddings. The dendrites were formed by two types of crystalline structures (fcc + hcp) with the same average chemical composition. The fcc structure underwent a thermal-induced partial martensitic transformation due to solidification rate in laser cladding that led to the formation of the hcp structure. However, the addition of boron promoted the formation of a eutectic phase in the interdendritic regions. The crystalline structure of the eutectic phase was consistent with a $(Cr.Fe)_2B$ boride phase, and the relative content of the boride phase increased with boron content up to 9% relative wt. The boride phase allowed increasing the microhardness of the laser cladding material about 1.5 times when comparing the sample without boron addition (LCA-B0, 291 ± 7 HV) and the sample with the highest boron addition (LCA-B10, 445 ± 42 HV). The increased content of the boride phase and the resultant microhardness due to boron addition allowed improving the abrasive wear-resistance of the alloy system prepared by laser cladding. The worn surface showed evidence of severe plastic deformation, micro-cutting and micro-ploughing as the main wear micromechanisms for the laser claddings. The high content of the boride phase in the laser cladding LCA-B10 allowed reducing the abrasive wear rate by more than 30% when compared with the alloy

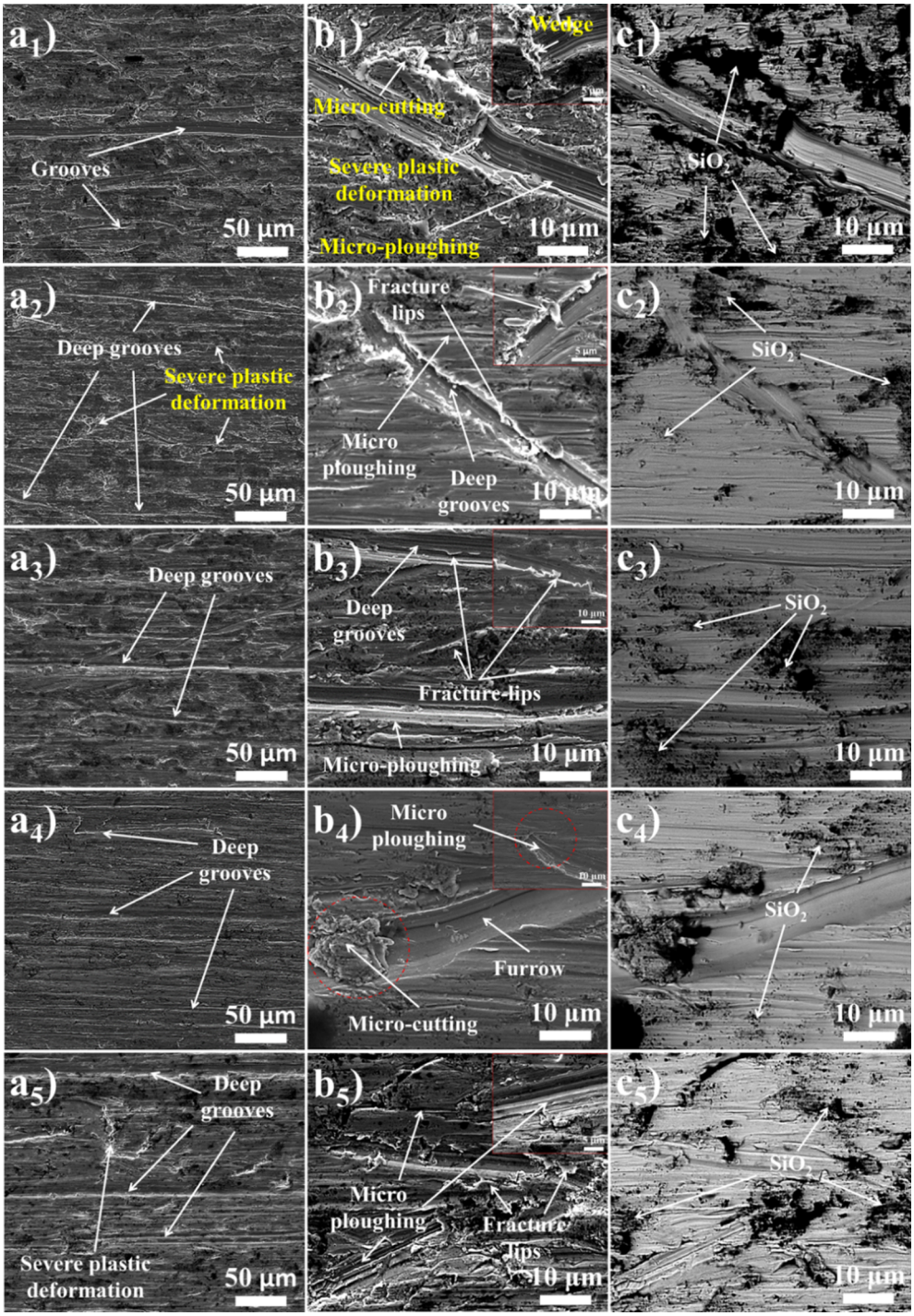

Fig. 9. Worn surface of the bare substrate (1), and laser claddings LCA-B0 (2), LCA-B3 (3), LCA-B5 (4) and LCA-B10 (5). ($a_{1\text{-}5}$) corresponds to a secondary-electrons image captured at low magnification, ($b_{1\text{-}5}$) shows an image captured in the same region at higher magnification, and ($c_{1\text{-}5}$) shows a back-scattered electron image captured at high magnification.

without boron content. Non-equiatomic $Fe_{50}Mn_{30}Co_{10}Cr_{10}$ alloys with the addition of boron are a promising material for surface engineering applications.

CRediT authorship contribution statement

Jose Y. Aguilar-Hurtado: Conceptualization, Methodology, Investigation, Writing - original draft. **Alejandro Vargas-Uscategui:** Conceptualization, Methodology, Resources, Writing - review and editing, Supervision. **Katherine Paredes-Gil:** Conceptualization, Writing - review & editing. **Rodrigo Palma-Hillerns:** Supervision, Resources. **Maria J. Tobar:** Resources, Investigation, Writing - review & editing. **Jose M. Amado:** Resources, Investigation, Supervision.

Acknowledgements

This work has been partially supported by CORFO Chile under grant Innova-10CEII9007 and by the CONICYT-Chile, under grant No. FB0809 “Technology Center for Mining”. J. Aguilar-Hurtado especially thanks CSIRO Chile International Centre of Excellence for his PhD

scholarship. The authors much acknowledge Dr. Aaron Seeber (CSIRO Manufacturing) for his assistance in the XRD analysis. The assistance of Dr. Fabiola Pineda (Corrosion and Wear Laboratory, Pontifical Catholic University of Chile) in the chemical composition analysis through the project Fondequip EQM160091 is kindly acknowledged. The authors would also like to thank the Faculty of Mathematical and Physical Sciences and the Mechanical Engineering Department at the University of Chile for its support in the development of this research.

Appendix A. Supplementary material

Supplementary data to this article can be found online at https://doi.org/10.1016/j.apsusc.2020.146084.

References

[1] C. Huang, Y. Zhang, R. Vilar, J. Shen, Dry sliding wear behavior of laser clad TiVCrAlSi high entropy alloy coatings on Ti – 6Al – 4V substrate, J. Mater. 41 (2012) 338–343, https://doi.org/10.1016/j.matdes.2012.04.049.
[2] D.B. Miracle, O.N. Senkov, A critical review of high entropy alloys and related concepts, Acta Mater. 122 (2017) 448–511, https://doi.org/10.1016/j.actamat.2016.08.081.
[3] F. Shu, B. Yang, S. Dong, H. Zhao, B. Xu, F. Xu, B. Liu, P. He, J. Feng, Effects of Fe-to-Co ratio on microstructure and mechanical properties of laser cladded FeCoCrBNiSi high-entropy alloy coatings, Appl. Surf. Sci. 450 (2018) 538–544, https://doi.org/10.1016/j.apsusc.2018.03.128.
[4] Z. Cai, X. Cui, Z. Liu, Y. Li, M. Dong, G. Jin, Microstructure and wear resistance of laser cladded Ni-Cr-Co-Ti-V high-entropy alloy coating after laser remelting processing, Opt. Laser Technol. 99 (2018) 276–281, https://doi.org/10.1016/j.optlastec.2017.09.012.
[5] J. Joseph, T. Jarvis, X. Wu, N. Stanford, P. Hodgson, D. Mark, Comparative study of the microstructures and mechanical properties of direct laser fabricated and arc-melted Al_xCoCrFeNi high entropy alloys, Mater. Sci. Eng., A 633 (2015) 184–193, https://doi.org/10.1016/j.msea.2015.02.072.
[6] X. Ji, H. Duan, H. Zhang, J. Ma, Slurry erosion resistance of laser clad $NiCoCrFeAl_3$ high-entropy alloy coatings, Tribol. Trans. 58 (2015) 1119–1123, https://doi.org/10.1080/10402004.2015.1044148.
[7] X.W. Qiu, C.G. Liu, Microstructure and properties of $Al_2CrFeCoCuTiNi_x$ high-entropy alloys prepared by laser cladding, J. Alloy. Compd. 553 (2013) 216–220, https://doi.org/10.1016/j.jallcom.2012.11.100.
[8] X.W. Qiu, Y.P. Zhang, C.G. Liu, Effect of Ti content on structure and properties of $Al_2CrFeNiCoCuTi_x$ high-entropy alloy coatings, J. Alloy. Compd. 585 (2014) 282–286, https://doi.org/10.1016/j.jallcom.2013.09.083.
[9] D. yang Lin, N. nan Zhang, B. He, G. wei Zhang, Y. Zhang, D. yuan Li, Tribological properties of FeCoCrNiAlBx high-entropy alloys coating prepared by laser cladding, J. Iron Steel Res. Int. 24 (2017) 184–189. doi:10.1016/S1006-706X(17)30026-2.
[10] N.A. Khan, B. Akhavan, H. Zhou, L. Chang, Y. Wang, L. Sun, M.M. Bilek, Z. Liu, High entropy alloy thin films of $AlCoCrCu_{0.5}FeNi$ with controlled microstructure, Appl. Surf. Sci. 495 (2019) 143560, https://doi.org/10.1016/j.apsusc.2019.143560.
[11] Q. Ye, K. Feng, Z. Li, F. Lu, R. Li, J. Huang, Y. Wu, Microstructure and corrosion properties of CrMnFeCoNi high entropy alloy coating, Appl. Surf. Sci. 396 (2017) 1420–1426, https://doi.org/10.1016/j.apsusc.2016.11.176.
[12] E.P. George, D. Raabe, R.O. Ritchie, High-entropy alloys, Nat. Rev. Mater. (2019), https://doi.org/10.1038/s41578-019-0121-4.
[13] Y. Yin, J. Zhang, Q. Tan, W. Zhuang, N. Mo, M. Bermingham, M.X. Zhang, Novel cost-effective Fe-based high entropy alloys with balanced strength and ductility, Mater. Des. 162 (2019) 24–33, https://doi.org/10.1016/j.matdes.2018.11.033.
[14] P. Wang, P. Huang, F.L. Ng, W.J. Sin, S. Lu, M.L.S. Nai, Z.L. Dong, J. Wei, Additively manufactured CoCrFeNiMn high-entropy alloy via pre-alloyed powder, Mater. Des. 168 (2019) 107576, , https://doi.org/10.1016/j.matdes.2018.107576.
[15] Z. Li, K.G. Pradeep, Y. Deng, D. Raabe, C.C. Tasan, Metastable high-entropy dual-phase alloys overcome the strength–ductility trade-off, Nature 534 (2016) 1–8, https://doi.org/10.1038/nature17981.
[16] Z. Li, C.C. Tasan, H. Springer, B. Gault, D. Raabe, Interstitial atoms enable joint twinning and transformation induced plasticity in strong and ductile high-entropy alloys, Sci. Rep. 7 (2017) 1–7, https://doi.org/10.1038/srep40704.
[17] J.B. Seol, J.W. Bae, Z. Li, J. Chan Han, J.G. Kim, D. Raabe, H.S. Kim, Boron doped ultrastrong and ductile high-entropy alloys, Acta Mater. 151 (2018) 366–376, https://doi.org/10.1016/j.actamat.2018.04.004.
[18] Z. Chong, W. Bingqian, W. Qianting, C. Dingning, D. Pinqiang, Microstructure and properties of $FeCrNiCoMnB_x$ high-entropy alloy coating prepared by laser cladding, Rare Met. Mater. Eng. 46 (2017) 2639–2644.
[19] V. Ferrari, W. Wolf, G. Zepon, F.G. Coury, M.J. Kaufman, C. Bolfarini, C.S. Kiminami, W.J. Botta, Effect of boron addition on the solidification sequence and microstructure of AlCoCrFeNi alloys, J. Alloy. Compd. 775 (2019) 1235–1243, https://doi.org/10.1016/j.jallcom.2018.10.268.
[20] C.S. Mahlami, X. Pan, Mechanical propierties and microstructure evaluation of high manganese steel alloyed with vanadium, Am. Inst. Phys. 020083 (2017), https://doi.org/10.1063/1.4990236.
[21] J.Y. Aguilar-Hurtado, A. Vargas-Uscategui, D. Zambrano-Mera, R. Palma-Hillerns, The effect of boron content on the microstructure and mechanical properties of $Fe_{50-X}Mn_{30}Co_{10}Cr_{10\ B}X$ (x = 0, 0.3, 0.6 and 1.7 wt%) multi-component alloys prepared by arc-melting, Mater. Sci. Eng. A. 748 (2019) 244–252, https://doi.org/10.1016/j.msea.2019.01.088.
[22] Z. Wang, I. Baker, Z. Cai, S. Chen, J.D. Poplawsky, W. Guo, The effect of interstitial carbon on the mechanical properties and dislocation substructure evolution in $Fe_{40.4}Ni_{11.3}Mn_{34.8}Al_{7.5}Cr_6$ high entropy alloys, Acta Mater. 120 (2016) 228–239, https://doi.org/10.1016/j.actamat.2016.08.072.
[23] Z. Wang, I. Baker, Interstitial strengthening of a f.c.c. FeNiMnAlCr high entropy alloy, Mater. Lett. 180 (2016) 153–156, https://doi.org/10.1016/j.matlet.2016.05.122.
[24] L. Xiaotao, L. Wenbin, M. Lijuan, L. Jinling, L. Jing, C. Jianzhong, Effect of boron on the microstructure, phase assemblage and wear properties of $Al_{0.5}$CoCrCuFeNi high-entropy alloy, Rare Met Mater. Eng. 45 (2016) 2201–2207, https://doi.org/10.1016/S1875-5372(17)30003-6.
[25] H. Zhang, Y. He, Y. Pan, Enhanced hardness and fracture toughness of the laser-solidified $FeCoNiCrCuTiMoAlSiB_{0.5}$ high-entropy alloy by martensite strengthening, Scr. Mater. 69 (2013) 342–345, https://doi.org/10.1016/j.scriptamat.2013.05.020.
[26] C. Li, J.C. Li, M. Zhao, L. Zhang, Q. Jiang, Microstructure and properties of $AlTiNiMnB_x$ high entropy alloys, Mater. Sci. Technol. 24 (2013) 376–378, https://doi.org/10.1179/174328408X275964.
[27] C. Zhang, G.J. Chen, P.Q. Dai, Evolution of the microstructure and properties of laser-clad $FeCrNiCoB_x$ high-entropy alloy coatings, Mater. Sci. Technol. 32 (2016) 1666–1672, https://doi.org/10.1080/02670836.2015.1138035.
[28] H. Zhang, H. Tang, Y.Z. He, J.L. Zhang, W.H. Li, S. Guo, Effect of heat treatment on borides precipitation and mechanical properties of $CoCrFeNiAl_{1.8}Cu_{0.7}B_{0.3}Si_{0.1}$ high-entropy alloy prepared by arc-melting and laser-cladding, JOM 69 (2017) 2078–2083, https://doi.org/10.1007/s11837-017-2381-z.
[29] Y. He, J. Zhang, H. Zhang, G. Song, Effects of different levels of boron on microstructure and hardness of $CoCrFeNiAl_xCu_{0.7}Si_{0.1}B_y$ High-entropy alloy coatings by laser cladding, Coatings 7 (2017) 7, https://doi.org/10.3390/coatings7010007.
[30] S. Nowotny, L.M. Berger, J. Spatzier, Coatings by laser cladding, Compr. Hard Mater. 1 (2014) 507–525, https://doi.org/10.1016/B978-0-08-096527-7.00018-0.
[31] W. Li, P. Liu, P.K. Liaw, Microstructures and properties of high-entropy alloy films and coatings: a review, Mater. Res. Lett. 6 (2018) 199–229, https://doi.org/10.1080/21663831.2018.1434248.
[32] H. Zhang, Y. Pan, Y.Z. He, J.L. Wu, T.M. Yue, S. Guo, Application prospects and microstructural features in laser-induced rapidly solidified high-entropy alloys, JOM 66 (2014) 2057–2066, https://doi.org/10.1007/s11837-014-1036-6.
[33] M.C.G.J. Yeh, P.K. Liaw, Y. Zhang, High-Entropy Alloys: Fundamentals and Applications, First edition, Springer International Publishing, Switzerland, 2016. doi:10.1007/978-3-319-27013-5.
[34] Y. Cai, Y. Chen, Z. Luo, F. Gao, L. Li, Manufacturing of $FeCoCrNiCu_x$ medium-entropy alloy coating using laser cladding technology, Mater. Des. 133 (2017) 91–108, https://doi.org/10.1016/j.matdes.2017.07.045.
[35] K. Zhang, X. Tian, M. Bermingham, J. Rao, Q. Jia, Y. Zhu, X. Wu, S. Cao, A. Huang, Effects of boron addition on microstructures and mechanical properties of Ti-6Al-4V manufactured by direct laser deposition, Mater. Des. 184 (2019) 108191, , https://doi.org/10.1016/j.matdes.2019.108191.
[36] A. Nouri, C. Wen, Surfactants in mechanical alloying/milling: a catch-22 situation, Crit. Rev. Solid State Mater. Sci. 39 (2014) 81–108, https://doi.org/10.1080/10408436.2013.808985.
[37] D.J.M. King, A.G. McGregor, Alloy Search And Predict (ASAP), http://34.209.81.123:8080/Systems.Htm. (2015) 8080.
[38] D.J.M. King, S.C. Middleburgh, A.G. McGregor, M.B. Cortie, Predicting the formation and stability of single phase high-entropy alloys, Acta Mater. 104 (2016) 172–179, https://doi.org/10.1016/j.actamat.2015.11.040.
[39] A. International, Standard test method for measuring abrasion using the dry sand / rubber wheel, ASTM Int. 04 (2014) 1–12, https://doi.org/10.1520/G0065-04R10.2.
[40] J.R. Davis, Handbook of thermal spray technology, Thermal Sp, ASM international, Materials Park, OH, 2004. www.asminternational.org.
[41] H. Zhang, Y. Pan, Y.Z. He, Synthesis and characterization of FeCoNiCrCu high-entropy alloy coating by laser cladding, Mater. Des. 32 (2011) 1910–1915, https://doi.org/10.1016/j.matdes.2010.12.001.
[42] F. Otto, A. Dlouhý, C. Somsen, H. Bei, G. Eggeler, E.P. George, The influences of temperature and microstructure on the tensile properties of a CoCrFeMnNi high-entropy alloy, Acta Mater. 61 (2013) 5743–5755, https://doi.org/10.1016/j.actamat.2013.06.018.
[43] J.A. Cabral Miramontes, J.D.O. Barceinas Sánchez, F. Almeraya Calderón, A. Martínez Villafañe, J.G. Chacón Nava, Effect of boron additions on sintering and densification of a ferritic stainless steel, J. Mater. Eng. Perform. 19 (2010) 880–884, https://doi.org/10.1007/s11665-009-9544-1.
[44] J. Ion, Laser processing of engineering materials: principles, procedure and industrial application, Elsevier Butterworth-Heinemann, Oxford, 2005.
[45] D. Tanigawa, N. Abe, M. Tsukamoto, Y. Hayashi, H. Yamazaki, Y. Tatsumi, M. Yoneyama, The effect of particle size on the heat affected zone during laser cladding of Ni–Cr–Si–B alloy on C45 carbon steel, Opt. Lasers Eng. 101 (2018) 23–27, https://doi.org/10.1016/j.optlaseng.2017.09.021.
[46] A.E.N.N. Greenwood, Chemistry of the elements, Second ed., Butterworth-Heinemann, 1997.
[47] S. Zanzarin, Laser cladding with powder, Doctoral thesis, University of Trento, 2015. https://core.ac.uk/download/pdf/35317589.pdf.
[48] G. Krauss, A.R. Marder, The morphology of martensite in iron alloys, Metall. Trans. 2 (1971) 2343–2357, https://doi.org/10.1007/BF02814873.
[49] P. Sahu, A.S. Hamada, R.N. Ghosh, L.P. Karjalainen, X-ray diffraction study on cooling-rate-induced γfcc→ εhcp martensitic transformation in cast-homogenized

Fe-26Mn-0.14C austenitic steel, Metall. Mater. Trans. A. 38A (2007) 1991–2000, https://doi.org/10.1007/s11661-007-9240-4.
[50] S. Silva, F. De Dafé, F.L. Sicupira, F. Cristina, S. Matos, N.S. Cruz, Effect of Cooling Rate on (ε , α ') Martensite Formation in Twinning / transformation-induced Plasticity Fe–17Mn–0.06C Steel, Mater. Res. 16 (2013) 1229–1236. doi:10.1590/S1516-14392013005000129.
[51] Y. Tian, A. Borgenstam, P. Hedström, A microstructural investigation of athermal and deformation-induced martensite in Fe-Cr-Ni Alloys, Mater. Today. Proc. 2 (2015) S687–S690, https://doi.org/10.1016/j.matpr.2015.07.376.
[52] Y. Tian, A. Borgenstam, P. Hedström, Comparing the deformation-induced martensitic transformation with the athermal martensitic transformation in Fe-Cr-Ni alloys, J. Alloy. Compd. 766 (2018) 131–139, https://doi.org/10.1016/j.jallcom.2018.06.326.
[53] K. Yamanaka, M. Mori, Y. Koizumi, A. Chiba, Local strain evolution due to athermal γ→ε martensitic transformation in biomedical CoCrMo alloys, J. Mech. Behav. Biomed. Mater. 32 (2014) 52–61, https://doi.org/10.1016/j.jmbbm.2013.12.019.
[54] A.L. Ramirez-Ledesma, E. Lopez-Molina, H.F. Lopez, J.A. Juarez-Islas, Athermal ε-martensite transformation in a Co-20Cr alloy: Effect of rapid solidification on plate nucleation, Acta Mater. 111 (2016) 138–147, https://doi.org/10.1016/j.actamat.2016.03.047.
[55] G. Bracq, M. Laurent-Brocq, L. Perrière, R. Pirès, J.M. Joubert, I. Guillot, The fcc solid solution stability in the Co-Cr-Fe-Mn-Ni multi-component system, Acta Mater. 128 (2017) 327–336, https://doi.org/10.1016/j.actamat.2017.02.017.
[56] Z. Wu, H. Bei, F. Otto, G.M. Pharr, E.P. George, Recovery, recrystallization, grain growth and phase stability of a family of FCC-structured multi-component equiatomic solid solution alloys, Intermetallics 46 (2014) 131–140, https://doi.org/10.1016/j.intermet.2013.10.024.
[57] G. Jin, Z. Cai, Y. Guan, X. Cui, Z. Liu, Y. Li, M. Dong, D. zhang, High temperature wear performance of laser-cladded FeNiCoAlCu high-entropy alloy coating, Appl. Surf. Sci. 445 (2018) 113–122, https://doi.org/10.1016/j.apsusc.2018.03.135.
[58] R.E. Schramm, R.P. Reed, Stacking fault energies of seven commercial austenitic stainless steels, Metall. Trans. A 6 (1975) 1345–1351, https://doi.org/10.1007/BF02641927.
[59] R.E. Schramm, R.P. Reed, Stacking fault energies of fcc Fe-Ni Alloys by X-ray diffraction line profile analysis, Metall. Trans. A 7A (1976) 359–363, https://doi.org/10.1007/BF02642831.
[60] C. Qiushi, D. Yong, Z. Junjia, L. Yiping, Microstructure and properties of $AlCoCrFeNiB_x$ (x = 0, 0.1, 0.25, 0.5, 0.75, 1.0) high entropy alloys, Rare Met. Mater. Eng. 46 (2017) 651–656, https://doi.org/10.1016/S1875-5372(17)30112-1.
[61] J.W. Yeh, Alloy design strategies and future trends in high-entropy alloys, JOM 65 (2013) 1759–1771, https://doi.org/10.1007/s11837-013-0761-6.
[62] Y. Zhou, D. Zhou, X. Jin, L. Zhang, X. Du, B. Li, Design of non-equiatomic medium-entropy alloys, Sci. Rep. 8 (2018) 1–9, https://doi.org/10.1038/s41598-018-19449-0.
[63] S. Guo, C.T. Liu, Phase stability in high entropy alloys : Formation of solid-solution phase or amorphous phase, Prog. Nat. Sci. Mater. Int. 21 (2011) 433–446, https://doi.org/10.1016/S1002-0071(12)60080-X.
[64] Y.J. Zhao, J.W. Qiao, S.G. Ma, M.C. Gao, H.J. Yang, M.W. Chen, Y. Zhang, A hexagonal close-packed high-entropy alloy: the effect of entropy, Mater. Des. 96 (2016) 10–15, https://doi.org/10.1016/j.matdes.2016.01.149.
[65] O.N. Senkov, J.D. Miller, D.B. Miracle, C. Woodward, Accelerated exploration of multi-principal element alloys with solid solution phases, Nat. Commun. 6 (2015) 1–10, https://doi.org/10.1038/ncomms7529.
[66] O.N. Senkov, J.D. Miller, D.B. Miracle, C. Woodward, Accelerated exploration of multi-principal element alloys for structural applications, CALPHAD: Comput. Coupling Phase Diagrams Thermochem. 50 (2015) 32–48, https://doi.org/10.1016/j.calphad.2015.04.009.
[67] N.D. Stepanov, N.Y. Yurchenko, M.A. Tikhonovsky, G.A. Salishchev, Effect of carbon content and annealing on structure and hardness of the CoCrFeNiMn-based high entropy alloys, J. Alloy. Compd. 687 (2016) 59–71, https://doi.org/10.1016/j.jallcom.2016.06.103.
[68] E. Sigolo, J. Soyama, G. Zepon, C.S. Kiminami, W.J. Botta, C. Bolfarini, Wear resistant coatings of boron-modified stainless steels deposited by plasma transferred arc, Surf. Coat. Technol. 302 (2016) 255–264, https://doi.org/10.1016/j.surfcoat.2016.06.023.
[69] K.H. Zum Gahr, Microstructure and wear of materials, Tribology series (10), Elsevier Science Publishers B.V, Amsterdam, The Netherlands, 1987.
[70] K.-H. Zum Gahr, Wear by hard particles, Tribol. Int. 31 (10) (1998) 587–596, https://doi.org/10.1016/S0301-679X(98)00079-6.
[71] J.B. Cheng, X.B. Liang, Z.H. Wang, B.S. Xu, Formation and mechanical properties of CoNiCuFeCr high-entropy alloys coatings prepared by plasma transferred arc cladding process, Plasma Chem. Plasma Process. 33 (2013) 979–992, https://doi.org/10.1007/s11090-013-9469-1.